Superconducting Ferromagnetic Nanodiamond

Zhang, G.; Samuely, T.; Xu, Z.; Jochum, J. K.; Volodin, A.; Zhou, S.; May, P. W.; Onufriienko, O.; Kačmarčík, J.; Steele, J. A.; Li, J.; Vanacken, J.; Vacík, J.; Szabó, P.; Yuan, H.; Roeffaers, M. B. J.; Cerbu, D.; Samuely, P.; Hofkens, J.; Moshchalkov, V. V.;

Originally published:

May 2017

ACS Nano 11(2017), 5358-5366

DOI: https://doi.org/10.1021/acsnano.7b01688

Perma-Link to Publication Repository of HZDR:

https://www.hzdr.de/publications/Publ-25850

Superconducting ferromagnetic nanodiamond

Gufei Zhang[1‡*], Tomas Samuely[2*], Zheng Xu[3*], Johanna Jochum[4], Alexander Volodin[4], Shengqiang Zhou[5], Paul W. May[6], Oleksandr Onufriienko[2], Jozef Kačmarčík[2], Julian A. Steele[7], Jun Li[8], Johan Vanacken[1], Jiri Vacík[9], Pavol Szabó[2], Haifeng Yuan[10], Maarten B. J. Roeffaers[7], Dorin Cerbu[1], Peter Samuely[2], Johan Hofkens[10], and Victor V. Moshchalkov[1§]

[1]INPAC-Insititute for Nanoscale Physics and Chemistry, KU Leuven, Celestijnenlaan 200D, B-3001 Heverlee, Belgium

[2]Centre of Low Temperature Physics, Institute of Experimental Physics, Slovak Academy of Sciences & Faculty of Science, P. J. Safarik University, 04001 Kosice, Slovakia

[3]School of Electrical and Computer Engineering, University of California, Davis, CA 95616, USA

[4]Solid State Physics and Magnetism Section, KU Leuven, B-3001 Heverlee, Belgium

[5]Helmholtz-Zentrum Dresden-Rossendorf, Institute of Ion Beam Physics and Materials Research, Bautzner Landstr. 400, 01328 Dresden, Germany

[6]School of Chemistry, University of Bristol, Bristol BS8 1TS, UK

[7]Centre for Surface Chemistry and Catalysis, KU Leuven, Celestijnenlaan 200F, B-3001 Heverlee, Belgium

[8]Research Institute of Superconductor Electronics, Nanjing University, 210093 Nanjing, China

[9]Nuclear Physics Institute, Academy of Sciences of the Czech Republic, 25068 Husinec-Rez, Czech Republic

[10]Department of Chemistry, KU Leuven, Celestijnenlaan 200F, B-3001 Heverlee, Belgium

[*]These authors contributed equally to this work.

[‡]e-mail: sp3.zhang@gmail.com; [§]e-mail: victor.moshchalkov@kuleuven.be

Abstract (Limit: 150 words; Count: 148 words)

Synthetic diamond is a promising candidate for the next-generation electronics due to its high breakdown voltage, thermal conductivity and tunable electronic properties upon doping. Superconductivity, discovered in boron-doped diamond, has extended the application range of this material even further. The magnetic properties of diamond, however, still remain rather unexploited, leaving the material an unmined treasure in the fields of magnetoelectronics and spintronics. Here we report on the observation of high-temperature ferromagnetism, giant positive magnetoresistance and anomalous Hall effect in hydrogenated boron-doped nanodiamond films. Our superconducting ferromagnetic nanodiamond films with a Curie temperature T_{Curie} > 400 K and a superconducting transition temperature T_c ~ 3 K, provide a powerful platform for investigating the competing interplay between ferromagnetism and superconductivity. Our research reveals the presence of an intriguing precursor phase, in which spin fluctuations intervene as a result of the interplay between the two antagonistic strongly correlated states.

Apart from being a symbol of wealth, prestige and love, diamond is increasingly being recognized as a material for science and technology, due to its unique properties and wide ranging applications [1]. The extraordinarily high breakdown voltage and thermal

conductivity, remarkable inertness to chemicals and contamination, and tunable electronic properties upon doping make diamond far more than a drilling tool for mining and machinery but also a promising candidate for the next-generation high-speed high-power electronics [1-3]. Cost-effective diamond films, prepared by the wafer-scale growth of diamond using chemical vapour deposition (CVD), can be easily integrated into the mature silicon industry and shaped into various high-technology devices [2-6].

The most effective known method to tune the electronic properties of diamond is to introduce substitutional boron dopants into this material. Upon doping, diamond undergoes the insulator-metal transition when the boron concentration reaches about 3×10^{20} cm^{-3} [7]. At even higher boron doping levels, diamond becomes superconducting [4,8]. These phase transitions in diamond can be roughly traced by its color change, i.e., light blue for semiconductive diamond, blue for diamond in the metallic regime, and deep blue/black for superconducting diamond. Despite the three-dimensional nature, significant variability in its physical properties has been observed in boron-doped diamond synthesized even under similar conditions, e.g., the broad range of the superconducting transition temperature T_c [4,7-12], the pronounced difference in the normal state resistivity [4,7-12], and anomalous resistance peaks and dips [2,7,9]. The cause of this variability lies in the specific synthesis method, growth mode and post-treatment of the diamond.

More than a superconductor, synthetic diamond can be also ferromagnetic. Theoretical modelling based on first principle calculations has demonstrated that the hydrogen incorporation can induce ferromagnetic behaviour in a metal-free diamond [13]. Meanwhile,

ferromagnetism has also been reported via bulk magnetization measurements for diamond that has been bombarded with nitrogen or carbon ions. This has been attributed to the bonding defects and mixture of sp^2/sp^3 carbon created by the ion damage [14,15]. Hydrogenation and sp^2/sp^3 defects have been generally employed to explain the intrinsic ferromagnetism observed in other carbonaceous substances as well, e.g., fullerenes [16], graphene [17], carbon nanotubes [18], and graphite [19].

Here we present our observations of the interplay between ferromagnetism and electrical transport in hydrogenated and heavily boron-doped nanodiamond (HBD) films, which has a Curie temperature of $T_{Curie} > 400$ K. Disfavored by the ferromagnetic ordering, the superconducting state still occurs in our HBD films at $T_c \sim 3$ K. The magnetization and resistivity of the HBD demonstrate an intimate correlation between each other at different temperatures, suggesting spin-dependent electrical transport and possible Cooper pairing due to spin fluctuations in the HBD films. Furthermore, the significant magnetic remanence well above room temperature, the anomalous Hall effect, and the giant positive low-field magnetoresistance, observed in our HBD films, open up new perspectives on the applications of this material in even wider range, e.g., magnetoelectronics, spintronics and magnetic field sensing.

The HBD films were deposited on SiO_2/Si substrates (undoped Si with 300 nm-thick SiO_2 on top) in a hot filament CVD reactor. Grazing incidence X-ray diffraction (GIXRD) was used for phase identification of the HBD films. Besides the Si (311) peak of the substrate, only diffraction peaks from polycrystalline diamond are found in the GIXRD spectrum (see

Figure 1a). Neutron depth profiling (NDP) analysis indicates that the film thickness is ~900 nm, and the boron concentration n_{boron} ~1.5 × 10^{21} cm^{-3}, well above the critical doping level for insulator-metal transition in diamond (see Fig. 1b) [7].

To analyze the hydrogenated surface, we investigated the HBD films by Raman scattering. Fig. 1c presents a characteristic Raman spectrum recorded from the HBD surface. The spectrum is partitioned into two areas of significance: low-frequency diamond vibrational modes, and a high-frequency band associated with carbon-hydrogen stretching vibrations originating from the hydrogenated surface. Note that similar spectra were obtained from both the undersurface (i.e., after the Si substrate had been chemically removed) and the upper surface of the HBD films. The two low-energy bands, centered at approximately 450 cm^{-1} and 1200 cm^{-1}, are caused by localized boron-boron dimer/cluster vibrations and the disorder-activation of otherwise forbidden diamond phonon density of states (PDOS), respectively [20,21]. In addition to the diamond peak located at 1332 cm^{-1}, a weak G band appears near 1500 cm^{-1} due to the presence of sp^2 carbon bonding at the diamond grain boundaries [22].

The high-energy modes between 2800 and 3100 cm^{-1} are the well-known signatures of a hydrogenated diamond surface and the stretching vibrations of carbon-hydrogen surface bonds [23-25]. The prominent features, which are resolved just above 2800 cm^{-1}, originate from a combination of symmetric and asymmetric carbon-hydrogen stretching with sp^3-hybridization [24]. A smaller peak at 3050 cm^{-1} also arises from carbon-hydrogen bonding, although from carbon in a sp^2-hybridization, and likely contributes to the bands at approximately 1500 cm^{-1} [26]. The relatively high strength of the carbon-hydrogen surface

Raman modes, as well as its presence over the entire HBD surface, confirms the successful hydrogenation of the sample surface.

We performed four-probe ac measurements on the HBD films to characterize their electrical transport properties. Fig. 1d shows the characteristic longitudinal thermoresistivity $\rho_{xx}(T)$ of the HBD films in different applied magnetic fields B. In zero magnetic field, when lowering T from 320 K, the resistivity decreases and reaches a minimum at about 100 K. Further decrease of T brings about a steep increase of $\rho_{xx}(T)$ within the temperature window of 30 - 100 K. As a result, the $\rho_{xx}(T)$ curve demonstrates a sharp dip at about100 K. Below 30 K, a slight increase in $\rho_{xx}(T)$ is followed by the resistive superconducting transition with T_c^{offset} = 3 K (T_c^{offset} is the offset critical temperature at which ρ drops to 0). Note that similar $\rho_{xx}(T)$ dips with much smaller amplitude have been previously reported for boron-doped diamond films grown by microwave plasma-enhanced CVD [7]. Both the superconducting state at low temperature and the anomalous $\rho_{xx}(T)$ dip at high temperature are suppressed by the applied magnetic field (see Fig. 1d).

Based on the magnetic field dependence of $\rho_{xx}(T)$, we constructed the $\mu_0 H_{c2}$-T phase diagram for the superconducting state (see Supplementary Section I). A quadratic fit to the $\mu_0 H_{c2}$-T phase boundary yields $\mu_0 H_{c2}(0\ \mathrm{K})$ = 4.3 T and thus the Ginzburg-Landau coherence length $\xi_{GL} = [\Phi_0/2\pi H_{c2}(0\ \mathrm{K})]^{1/2}$ = 8.7 nm with $\Phi_0 = h/2e$ being the flux quantum. The same $\mu_0 H_{c2}(0\ \mathrm{K})$ and ξ_{GL} values are obtained from the linear fit to the phase boundary, following the standard relationship for a dirty type-II superconductor $H_{c2}(0\ \mathrm{K}) = -0.69 T_c (dH/dT)\big|_{Tc}$.

Consistent with the $\rho_{xx}(T)$ data, giant positive magnetoresistance (PMR) was observed when measuring the longitudinal resistivity as a function of magnetic field $\rho_{xx}(B)$ at temperatures around the $\rho_{xx}(T)$ dip (see Figure 2a). The largest PMR = $[\rho_{xx}(B)-\rho_{xx}|_{B=0}]/\rho_{xx}|_{B=0}$ goes up to nearly 90% at about 83 K when B = 8 T (see Supplementary Section II). The strong temperature dependence of the electrical transport properties is also apparent in the Hall effect measurements. Fig. 2b shows the transverse resistivity $\rho_{xy}(B)$ measured at different temperatures. Below 30 K, linear $\rho_{xy}(B)$ behaviour is found at the normal state, while anomalous Hall effect (AHE) appears at high temperatures where the $\rho_{xx}(T)$ dip is located.

AHE has been generally observed in ferromagnetic semiconductors and oxides [27], and its origin still remains an open question. The nonlinear $\rho_{xy}(B)$ behaviour has been either attributed to the magnetic field-dependent ratio between the mobility of holes and electrons based on the compensation effects [28], or interpreted as a result of superposition of the ordinary Hall effect and the magnetic scattering mechanism [29]. Note that the two techniques involved in our preparation of the HBD films, i.e., boron doping and hydrogenation, are both well-known approaches to achieve *p*-type conduction in diamond [30]. Furthermore, although the intergrain sp^2 medium can be a source of electrons, no AHE so far has been reported for other granular diamond systems which are also rich in intergrain sp^2 phases. The AHE observed in our HBD films is, therefore, most likely due to the magnetic scattering in the samples.

Based on the $\rho_{xx}(B)$ and $\rho_{xy}(B)$ data, we deduced the mean free path $l = \hbar k_F \tau / m^*$ of the free carriers by assuming contributions from *p*-type carriers only. Here $\hbar$ is the Dirac constant,

$k_F = (3\pi^2 n)^{1/3}$ is the Fermi wave vector under a spherical Fermi surface approximation with n being the carrier density, τ the mean free time, and m^* the effective mass of the carriers. To eliminate τ/m^*, the Boltzmann conductivity $\sigma = nq^2\tau/m^*$ is introduced into the expression for l

$$l = \hbar\left(3\pi^2\right)^{1/3}\frac{\sigma}{n^{2/3}q^2} = \frac{\hbar\left(3\pi^2\right)^{1/3}R_H{}^{2/3}}{q^{4/3}\rho_{xx}} \quad (1)$$

where q is the elementary charge, and R_H is the Hall coefficient [31]. This calculated value of l is plotted as a function of T and B in Fig. 2c, to which the $\rho_{xx}(T)|_{B=0}$ curve is added for reference. Our data clearly show that the dramatic change of l around 100 K is responsible for the formation of the anomalous $\rho_{xx}(T)$ dip. Further evidence for this is given by the systematic suppression of the l peak and the $\rho_{xx}(T)$ dip in different magnetic fields (see Fig. 1d and Fig. 2c).

When looking into the underlying physics of the anomalous $\rho_{xx}(T)$ dip via bulk magnetization measurements, ferromagnetism was found in our HBD films. Figure 3a shows the magnetization hysteresis loops $M(H)$ before subtraction of the linear diamagnetic background of the substrate. After eliminating the substrate signal and normalizing the HBD signal to the HBD mass, the low-field $M(H)$ of significance is plotted in Fig. 3b and Fig. 3c to provide a clear view of the temperature-induced evolution of the central peak, the virgin curve and the coercivity. The $M(H)$ loops, measured at $T < T_c^{offset}$, demonstrate a central peak superimposed on a ferromagnetic background around zero field. The central peak diminishes as the temperature is increased, leaving the ferromagnetic signal behind at higher temperatures (see Fig. 3b and Fig. 3c). A similar scenario takes place in the virgin curve as

well. The V-shaped virgin curve diminishes and ends up with a conventional ferromagnetic feature above T_c^{offset}. Analysis of the virgin curves yields a lower critical field of $\mu_0 H_{c1} \sim 0.5$ mT at $T = 0$ (see Supplementary Section I).

As shown in the inset to Fig. 3d, a sudden increase begins in the coercive field $\mu_0 H_{CF}$ when the temperature is lowered to T_c^{offset}. In contrast to the data for a nonmagnetic superconductor [12], the zero-field cooling (ZFC) and field cooling (FC) curves of our HBD, measured at 5 mT, remain separated from each other throughout the entire temperature range of 1.8 - 400 K (see Fig. 3d), suggesting the presence of ferromagnetism with $T_{Curie} > 400$ K in addition to the superconducting transition around $T_c^{offset} = 3$ K. We measured the ZFC and FC magnetization as a function of temperature in different applied magnetic fields (see Fig. 3e). When increasing the magnetic field, the superconducting state is gradually suppressed and the ZFC and FC curves start merging at high temperatures. Our bulk magnetization data clearly reveal the coexistence of superconductivity and ferromagnetism in the HBD films.

To gain further insight into the ferromagnetism and its competing interplay with the superconductivity in the HBD films, we performed direct local measurements with magnetic force microscopy (MFM) and scanning tunneling microscopy/spectroscopy (STM/S), respectively. Granular diamond films such as our HBD generally have an upper surface roughness comparable to the film thickness due to the growth mode of this material. To minimize the influence of the surface roughness on the local measurements, the MFM and STM/S measurements were carried out on the relatively flat undersurface.

Direct evidence for the presence of ferromagnetism in our HBD was provided by the MFM measurements at room temperature. Figures 4a-c display the topography of a 10 μm × 10 μm undersurface and the corresponding MFM images of this area, respectively. Since MFM measures the vertical component of the force gradient between the sample and the tip, it is sensitive to the strength and polarity of near-surface stray fields produced by ferromagnetic samples. As shown in Fig. 4a-c, our MFM data demonstrate clear magnetic contrasts in different magnetic fields, and show no correlation between the topography and the magnetic structures, revealing the genuine ferromagnetism of the HBD.

The origin of the ferromagnetism in metal-free carbon allotropes still remains a subject of debate. It was first argued that bonding defects in sp^2 and sp^3 mixtures are responsible for the ferromagnetism observed in bombarded graphite and diamond [14,15]. Later, the ferromagnetism in carbon-based materials was found to be intrinsic and linked to hydrogen at the surface, based on detailed studies using X-ray magnetic circular dichroism [19]. In our HBD films, both bonding defects and hydrogen are present. The grain boundaries of polycrystalline diamond are known to be rich in sp^2 and sp^3 mixtures [12]. Taking into account the absence of ferromagnetism in polycrystalline bulk diamond prepared using the high-temperature high-pressure method (a synthetic process in which no hydrogen is involved) [12], hydrogen incorporation at the surfaces and interfaces is more likely to be the cause of the ferromagnetism observed in our HBD films.

To gain further insight into the competing interplay between the superconductivity and ferromagnetism in the HBD films, we simultaneously acquired the conductance map and the

topography of the HBD undersurface with STM/S in the current-imaging tunneling spectroscopy (CITS) mode [32] and in constant-current mode, respectively. By normalizing the differential conductance spectra $G(V_b) = dI/dV$ to a value far outside the superconducting gap, and collecting the $G_{zb} = G(V_b = 0)$ values, we built up so-called zero-bias conductance G_{zb} maps in combination with the corresponding topography (see Figure 5a, for example).

Fig. 5a-c show the magnetic field-induced evolution of the G_{zb} map from a characteristic area at 0.5 K. When $B = 0$ T, the G_{zb} is rather homogeneous and equal to zero, indicating full superconducting gap across the whole area (see Fig. 5a). Upon applying magnetic field, the G_{zb} map separates into two main regions, a bluish one with lower G_{zb} and a reddish one with higher G_{zb} (see Fig. 5b). The spatial variations of G_{zb} (the modulations of the superconducting order parameter Δ) have also previously been observed in non-ferromagnetic diamond, and were explained as resulting from the granular disorder and/or intragrain "uniform" disorder [12]. In our superconducting ferromagnetic HBD, variations of the local magnetic structure (see Fig. 4b and 4c) can also be a cause of this phenomenon. By further increasing B, the superconductivity in the whole scanned area was gradually suppressed, resulting in $G_{zb} = 1$ at nearly every spot (see Fig. 5c).

Fig. 5d shows the normalized differential conductance spectra $G_{norm}(V_b)$ recorded from a characteristic spot ⊕ (see Fig. 5a-c). The gradual destruction of superconductivity in higher magnetic fields is responsible for the in-gap states and the suppression of the coherence peaks. The magnetic field-induced evolution of G_{zb} is summarized in Fig. 5e. In all cases, G_{zb} remains zero below ~0.05 T (see Fig. 5e and Supplementary Section III), and then increases

linearly to almost unity at higher magnetic fields, i.e., at ~0.2 T for the ⊗ region and at ~0.3 T for the ⊕ region. Note that the effective shielding of the applied magnetic field at $B \leq 0.05$ T cannot be due to Meissner expulsion, since this field is larger than $\mu_0 H_{c1} \sim 0.5$ mT by two orders of magnitude. In contrast, magnetic field compensation can give rise to the shielding effect, i.e., the applied magnetic field is compensated by the stray field of the ferromagnetic HBD.

We performed STS measurements over several areas across the whole sample surface and found no superconductivity above 0.4 T, which clearly demonstrates that the surface critical field of our HBD is one order of magnitude smaller than the bulk critical field of ~4 T, as obtained from the $\rho_{xx}(T)$ measurements (see Fig. 1d). We also emphasize that for a non-ferromagnetic diamond with similar T_c^{offset} and normal-state resistivity ρ_{norm} ($T_c^{offset} \sim 3$ K; $\rho_{norm} \sim 18$ μΩ m), the surface critical field is of the same order of magnitude as the bulk value ~ 4-5 T [12].

As already discussed above, the critical magnetic field of the HBD surface is unusually small in comparison with the bulk critical magnetic field. The same conclusion can be drawn when taking into account the superconducting gap size 2Δ and the local critical temperature T_c(local). We measured the temperature-induced evolution of $G(V_b)$ at $B = 0$ T, from which the $\Delta(T)$ values are deduced. The $\Delta(T)$ of spots ⊗ and ⊕ are then fitted by a BCS-like $\Delta(T)$ dependence in Fig. 5f. Despite the difference between their critical field (see Fig. 5a-c), both spots have the same $\Delta(0\text{ K}) = 1.45$ meV and T_c(local) = 7 K within the limits of experimental error. Similar Δ and T_c(local) values were observed across the whole sample.

Accordingly, in the absence of ferromagnetism, an applied magnetic field higher than 10 T will be needed to fully suppress the superconductivity at the HBD surface [9]. This is obviously not the case, as evidenced by our STM/S measurements in different applied magnetic fields (see Fig. 5a-e). Notably, the ratio $2\Delta(0\ \mathrm{K})/k_{\mathrm{B}}T_{\mathrm{c}}(\mathrm{local}) = 4.8$ is 36% larger than the conventional BCS theory value, meaning that our HBD films are situated in the strong coupling regime [33].

The two antagonistic strongly correlated states, superconductivity and ferromagnetism, are not electronically independent from each other but intimately entangled in our HBD. When plotting the electrical transport and magnetization data together (see Figure 6a), an intimate correlation between the $\rho_{xx}(T)$ and $M(T)$ behaviors is found in different temperature windows. Above 100 K, our HBD demonstrates an overall ferromagnetic state with parallel-aligned spins (see Fig. 6b), and the transport of carriers with well aligned spins results in the metallic state (see the red-shadowed regime in Fig. 6a). At low temperatures, besides boron-doping-induced superconductivity in diamond, Cooper pairing of the carriers with antiparallel-aligned spins at domain walls can also contribute to the formation of the superconducting state (see Fig. 6c and the blue-shadowed regime in Fig. 6a) in the framework of the so-called domain wall superconductivity as suggested by Anderson and Suhl [34,35].

In the case that the same carriers are involved in the development of the two phases as illustrated in Fig. 6b and 6c, a precursor phase will be required for the antiferromagnetic arrangement of the magnetic domains at low temperatures. The green-shadowed regime in Fig. 6a is exactly the precursor phase, in which misorientation of the spins takes place (see Fig.

6b), as evidenced by the decrease in $M(T)$ when lowering the temperature. Although it is irrational to attribute the negative temperature coefficient of $\rho_{xx}(T)$ to the spin misorientation alone, since after all our HBD is a granular disordered system and the granular disorder-correlated localization effect also plays an essential role in determining the electrical transport at low temperatures [36], the antiferromagnetic arrangement of the magnetic domains is proven to be genuine by the presence of the precursor phase in the HBD.

In conclusion, the significant magnetic remanence well above room temperature, the giant positive low-field magnetoresistance (~90% above liquid-nitrogen temperature), and the pronounced anomalous Hall effect, make our HBD a promising candidate for applications in not only power electronics and microelectronics but also magnetoelectronics, spintronics and magnetic field sensing. The ferromagnetic ordering with $T_{Curie} > 400$ K and the superconducting ordering with $T_c \sim 3$ K, proven to be electronically entangled with each other, make our HBD also an interesting platform for investigating the competing interplay between the two antagonistic strongly correlated states of condensed matter. Our data indicate the presence of a precursor phase, in which spin fluctuations intervene and contribute to the superconducting transition at lower temperatures. The significant difference between the starting temperature of this precursor phase (~ 100 K) and T_c, however, raises an intriguing question, i.e., how does a ferromagnetic superconductor such as our HBD "foresee" its low-temperature superconducting "fate" and start "preparing" for the superconducting transition via antiferromagnetic arrangements of the magnetic domains at a much higher temperature? More thorough local measurements and theoretical modeling are needed to solve this mysterious problem.

Methods

Synthesis of the HBD films with hot filament CVD. The HBD films were synthesized in a hot filament CVD reactor. SiO_2/Si substrates (undoped Si with 300 nm-thick SiO_2 on top) were seeded with diamond powders (Ø ~ 15-25 nm), to generate nucleation sites for the diamond growth at 800 °C. A gas mixture, 0.6% CH_4 in H_2, was thermally dissociated at 2200 °C as the source of reactive hydrocarbon species. Boron doping was obtained by adding diborane (B_2H_6) to the gas mixture with a B_2H_6/CH_4 ratio of 5%. After 1 h deposition, the resulting boron-doped nanodiamond films had a thickness of ~900 nm and a mean grain size of ~800 nm (see inset, Figure 1d). The interface between diamond crystallites is believed to be only a few atoms thick, and composed of a mixture of hydrogenated and unhydrogenated sp^2 and sp^3 carbon. Following deposition, the CH_4 and B_2H_6 gases were switched off while the sample remained under the filaments for one minute in pure hydrogen gas, before being cooled to room temperature under H_2. This ensured that the surface was hydrogen terminated [1]. The as-deposited diamond films were directly used for our structural analysis (GIXRD, NDP and Raman scattering), electrical transport and bulk magnetization measurements. To perform Raman scattering, MFM and STM/S measurements on the relatively flat undersurface of the HBD, the samples were marinated in 40% HF analar for 3 hours to etch out the SiO_2 in between the HBD and Si. The freestanding HBD films, removed from the substrate, were then flipped over and placed onto nonmagnetic substrate for relevant experiments.

Phase identification of the HBD films by GIXRD. The GIXRD spectrum was collected by using a Panalytical X'pert Pro diffractometer with an incident angle of 2° for the incoming X-

ray.

Determination of the boron doping level by NDP. Based on the thermal neutron-induced $^{10}B(n,\alpha)^{7}Li$ reaction, NDP was used to measure the depth dependence of the boron concentration [36].

Confirmation of the HBD surface hydrogenation by Raman scattering. Unpolarised micro-Raman scattering data were acquired in a quasi-backscattering configuration from the sample surface, employing a 20mW argon ion gas laser operating at 488 nm, with the beam focused using a Zeiss 100×/1.3 oil objective. Raman spectra were dispersed via a triple grating system (300g/mm:300g/mm:500g/mm) in a subtractive configuration, and the Raman signals were recorded using a liquid-nitrogen-cooled CCD detector. The correct instrument calibration was verified by checking the position of the Si band at ±520.7 cm^{-1}.

Electrical transport measurements. The electrical transport properties of the HBD films were characterized in a Heliox ^{3}He cryostat (Oxford Instruments) and a physical property measurement system (Quantum Design). The same results were obtained from the four-probe ac and dc measurements on the HBD. No difference was seen between the data measured in a parallel magnetic field and in a perpendicular field, indicating that our HBD films are in the three-dimensional regime.

Bulk magnetization measurements. Magnetometry of the HBD was performed by using a MPMS3 (Quantum Design) system in Dresden for preliminary checks and another MPMS3 (Quantum Design) system in Leuven for detailed characterization. No difference was seen between the data measured in a parallel magnetic field and in a perpendicular field.

Magnetic force microscopy (MFM). MFM measurements were performed with a Dimension 3100D scanning probe microscope (Bruker) operated in the tapping lift mode. Commercial

MFM probes PPP-MFMR (Nanosensors) with a remanence tip magnetization of ~300 emu/cm^3 aligned along the tip axis were used. During the scanning procedure, the MFM probe-cantilever resonant frequency (~60 kHz) shifts were proportional to vertical gradients of the magnetic forces acting on the tip. These frequency shifts φ (in degree) were detected as the cantilever's phase of oscillation relative to its actuator drive. In the tapping lift mode, the first scan was performed to obtain the topography by scanning the tip near the sample surface. During the second scan, MFM lifted the tip and maintained a constant tip-sample distance of ~50 nm. Thus, from the second scan, a topography-free MFM signal was acquired.

Scanning tunneling microscopy/spectroscopy (STM/S). STM/S experiments were carried out by means of a sub-Kelvin STM system. Atomically sharp STM tips were formed *in situ* by controlled contact of the Au tip with a clean Au surface at cryogenic temperatures [37]. Since the Au tip has a constant density of states, the acquired $G(V_b)$ spectra represent the local density of states (LDOS) of the sample, and the G_{zb} maps reflect the spatial variation of the superconducting gap. Surface topography was acquired in the constant current mode with tunneling resistance of 500 kΩ. Magnetic fields were applied perpendicular to the MCD surface for the field-induced evolution of $G(V_b)$.

References

1. May, P. W. Diamond thin films: a 21-st century material. *Phil. Trans. R. Soc. A* **358**, 473–495 (2000).

2. Zhang, G. *et al*. Bosonic anomalies in boron-doped polycrystalline diamond. *Phys. Rev. Applied* XXX (2016).

3. Gajewski, W. *et al*. Electronic and optical properties of boron-doped nanocrystalline

diamond films, *Phys. Rev. B* **79**, 045206 (2009).

4. Takano, Y. *et al*. Superconductivity in diamond thin films well above liquid helium temperature. *Appl. Phys. Lett.* **85**, 2851–2853 (2004).

5. Mandal, S. *et al*. The diamond superconducting quantum interference device. *ACS Nano* **5**, 7144–7148 (2011).

6. Hantschel, T. *et al*. Conductive diamond tips with sub-nanometer electrical resolution for characterization of nanoelectronics device structures, *Phys. Stat. Sol. A* **206**, 2077–2081 (2009).

7. Klein, T. *et al*. Metal-insulator transition and superconductivity in boron-doped diamond. *Phys*. *Rev*. *B* **75,** 165313 (2007).

8. Ekimov, E. A. *et al*. Superconductivity in diamond. *Nature* **428,** 542–545 (2004).

9. Zhang, G., Zeleznik, M., Vanacken, J., May, P. W. & Moshchalkov, V. V. Metal-bosonic insulator-superconductor transition in boron-doped granular diamond. *Phys*. *Rev*. *Lett*. **110,** 077001 (2013).

10. Bustarret, E. *et al*. Dependence of the superconducting transition temperature on the doping level in single-crystalline diamond films, *Phys. Rev. Lett.* **93**, 237005 (2004).

11. Bustarret, E. Superconducting diamond: an introduction, *Phys. Stat. Sol. (a)* **205**, 997–1008 (2008).

12. Zhang, G. *et al*. Global and local superconductivity in boron-doped granular diamond, *Adv. Mater.* **26**, 2034–2040 (2014).

13. Kenmochi, K., Sato, K., Yanase, A. & Katayama-Yoshida, H. Materials design of ferromagnetic diamond. *Jpn*. *J*. *Appl*. *Phys*. **44,** L51–L53 (2005).

14. Talapatra, S. *et al*. Irradiation-induced magnetism in carbon nanostructures. *Phys*. *Rev*.

Lett. **95,** 097201 (2005).

15. Remes, Z. *et al*. Ferromagnetism appears in nitrogen implanted nanocrystalline diamond films. *J. Magn. Magn. Mater*. **394,** 477–480 (2015).

16. Makarova, T. L. Magnetic properties of carbon structures. *Semiconductors* **38,** 615–638 (2004).

17. Wang, Y. *et al*. Room-temperature ferromagnetism of graphene. *Nano Lett*. **9,** 220–224 (2009).

18. Yan, D. *et al*. Ferromagnetism of double-walled carbon nanotubes. *Appl. Phys. Lett*. **96,** 242503 (2010).

19. Ohldag, H. *et al*. The role of hydrogen in room-temperature ferromagnetism at graphite surfaces. *New J. Phys*. **12,** 123012 (2010).

20. Bernard, M., Baron, C. & Deneuville, A. About the origin of the low wave number structures of the Raman spectra of heavily boron doped diamond films. *Diamond Relat. Mater.* **13**, 896–899 (2004).

21. Bourgeois, E., Bustarret, E., Achatz, P., Omnès, F. & Blase, X. Impurity dimers in superconducting B-doped diamond: experiment and first-principles calculations. *Phys. Rev. B* **74**, 094509 (2006).

22. Sun, Z., Shi, J., Tay, B. & Lau, S. UV Raman characteristics of nanocrystalline diamond films with different grain size. *Diamond Relat. Mater.* **9**, 1979–1983 (2000).

23. Lee, S.-T. & Apai, G. Surface phonons and CH vibrational modes of diamond (100) and (111) surfaces. *Phys. Rev. B* **48**, 2684–2693 (1993).

24. Ushizawa, K. *et al*. Surface-enhanced Raman spectroscopic study of hydrogen and deuterium chemisorption on diamond (111) and (100) surfaces. *Phys. Rev. B* **60**, R5165–

R5168 (1999).

25. Bernard, M., Deneuville, A. & Bustarret, E. Detection of CH_x bonds from micro raman spectroscopy on polycrystalline boron doped diamond electrodes. *Diamond Relat. Mater.* **11**, 662–666 (2002).

26. Lafosse, A., Hoffman, A., Bertin, M., Teillet-Billy, D. & Azria, R. Density-of-states effect on surface and lattice vibrational modes in hydrogenated polycrystalline diamond. *Phys. Rev. B* **73**, 195308 (2006).

27. Nagaosa, N., Sinova, J., Onoda, S., MacDonald, A. H. & Ong, N. P. Anomalous Hall effect. *Rev. Mod. Phys.* **82**, 1539–1592 (2010).

28. Jakob, G., Martin, F., Westerburg, W. & Adrian, H. Evidence of charge-carrier compensation effects in $La_{0.67}Ca_{0.33}MnO_3$. *Phys. Rev. B* **57**, 10252 (1998).

29. Wagner, P., Mazilu, D., Trappeniers, L., Moshchalkov, V. V. & Bruynseraede, Y. Anomalous Hall effect in thin films of $Pr_{0.5}Sr_{0.5}MnO_3$. *Phys. Rev. B* **55**, R14721 (1997).

30. Kawarada, H. Hydrogen-terminated diamond surfaces and interfaces. *Surf. Sci. Rep.* **26**, 205–259 (1996).

31. Graham, M. R., Adkins, C. J., Behar, H. & Rosenbaum, R. Experimental study of the Ioffe-Regel criterion for amorphous indium oxide films. *J. Phys.: Condens. Matter* **10**, 809–819 (1998).

32. Hamers, R. J., Tromp, R. M. & Demuth, J. E. Surface electronic structure of Si(111)-(7×7) resolved in real space. *Phys. Rev. Lett.* **56,** 1972–1975 (1986).

33. Onufriienko, O. *et al*. Superconducting density of states in B-doped diamond. *Acta. Phys. Pol. A*, in press (2017).

34. Anderson, P. W. & Suhl, H. Spin alignment in the superconducting state. *Phys. Rev.* **116**,

898–900 (1959).

35. Buzdin, A. I. & Mel'nikov, A. S. Domain wall superconductivity in ferromagnetic superconductors. *Phys. Rev. B* **67**, 020503(R) (2003).

36. Zhang, G. *et al*. Role of grain size in superconducting boron-doped nanocrystalline diamond thin films grown by CVD. *Phys*. *Rev*. *B* **84,** 214517 (2011).

37. Samuely, T. *et al*. Enhanced superconductivity in nanosized tips of scanning tunnelling microscope. *Acta*. *Phys*. *Pol*. *A* **118,** 1038 (2010).

Acknowledgements

G.Z., J. Van., D.C. and V.V.M. acknowledge support from the Methusalem Funding by the Flemish Government. G.Z. and H.Y. are postdoctoral research fellows of the FWO (Research Foundation-Flanders). G.Z., J.J. and J. Van. thank the Hercules Foundation. T.S., O.O., J.K., P.Sz. and P.S. are supported by APVV-0036-11, APVV-14-0605, VEGA 1/0409/15, VEGA 2/0149/16 and EU ERDF-ITMS 26220120005. S.Z. acknowledges support from the Helmholtz Association (Grant No. VH-NG-713). P.W.M. thanks the UK EPSRC for funding. J.Vac. thanks the Grant Agency of CR [P108-12G-108] for support. M.B.J.R. acknowledges financial support from the FWO (Grant G.0962.13, G.0B39.15), KU Leuven Research Fund (C14/15/053) and the European Research Council for ERC-Stg LIGHT [307523].

Author contributions

G.Z., J.Van. and V.V.M. conceived the study and designed the experiment. Z.X. and P.W.M. prepared the diamond samples. T.S., O.O., P.Sz. and P.S. carried out scanning tunneling microscopy/spectroscopy measurements. J.J., S.Z. and G.Z. measured the bulk magnetization

of the samples. A.V. performed magnetic force microscopy measurements. G.Z., J.K., J.Van., J.L., D.C. and V.V.M. did the electrical transport measurements and analyzed the data. J.S., H.Y., M.R. and J.H. executed Raman scattering measurements and took the scanning electron micrographs. J.Vac. analyzed the samples with neutron depth profiling. G.Z. and V.V.M. wrote the paper, with contributions from the co-authors.

Additional information

Correspondence and requests for materials should be addressed to G.Z. and V.V.M.

Competing financial interests

The authors declare that they have no competing financial interests.

Figure legends

Figure 1 | Structural analysis and the longitudinal thermoresistivity $\rho_{xx}(T)$ of the hydrogenated boron-doped nanodiamond (HBD) films. a, In the grazing incident X-ray diffraction spectrum, only diffraction peaks from diamond (colored stars) and the Si substrate (inverted triangle) are found, revealing the polycrystalline structure of the HBD and the absence of impurity phases. **b**, Neutron depth profiling analysis indicates that the HBD film thickness is about 900 nm, and the boron concentration is around 1.5×10^{21} cm^{-3}. **c**, Raman scattering spectrum, excited with a 488 nm laser, confirms the successful surface hydrogenation of the HBD. For clarity, the two regions of significance, i.e., the boron-doped nanodiamond (BND) modes and the carbon-hydrogen (C-H) surface modes, are emphasized, with the latter being

resolved and rescaled (×4). B-B: boron-boron dimer/cluster vibrations. PDOS: the disorder-activation of otherwise forbidden diamond phonon density of states. For CH_x, x = 1, 2 and 3. **d**, $\rho_{xx}(T)$ demonstrates a resistive superconducting transition at low temperature with the offset critical temperature T_c^{offset} = 3 K and an anomalous dip at around 100 K. Both the superconducting transition and the anomalous dip are suppressed by applied magnetic fields. Inset: scanning electron micrograph displaying the granular morphology of the HBD.

Figure 2 | The longitudinal magnetoresistivity $\rho_{xx}(B)$, the transverse resistivity $\rho_{xy}(B)$ and the mean free path l of the HBD films. a, Giant positive magnetoresistance is observed in the temperature window, where the anomalous $\rho_{xx}(T)$ dip is located. **b**, In the same temperature window, $\rho_{xy}(B)$ demonstrates anomalous Hall effect. **c**, The mean free path, deduced from the $\rho_{xx}(B)$ and $\rho_{xy}(B)$ measurements, is plotted together with the anomalous $\rho_{xx}(T)$ dip. The l peak, suppressed in applied magnetic fields, takes responsibility for the formation of the $\rho_{xx}(T)$ dip.

Figure 3 | Magnetization versus applied magnetic field and temperature, indicating the presence of ferromagnetism with T_{Curie} > 400 K and the coexistent superconductivity with T_c ~ 3 K in the HBD. a, Magnetization hysteresis loops $M(H)$ measured at different temperatures for the substrate (SUB) and the HBD grown on the substrate (HBD+SUB). As evidenced by its linear $M(H)$, the substrate is simply diamagnetic throughout the entire temperature range. **b**, After

eliminating the diamagnetic background signal of the SUB, the $M(H)$ is normalized to the mass of the HBD. The $M(H)$, measured below 3 K, demonstrates a central peak and a V-shaped virgin curve which are superimposed on a ferromagnetic background. Ferromagnetic $M(H)$ is seen up to 400 K. **c**, The central peak and the V-shaped virgin curve smear out at higher temperatures, leaving behind the ferromagnetic signal above 3 K. **d**, Magnetization versus temperature $M(T)$ measured in zero-field-cooling (ZFC) and field-cooling (FC) processes. The ZFC and FC curves show a superconducting transition at about 3 K (the dash-dotted line), and remain separated from each other up to 400 K. Inset: coercive field versus temperature $\mu_0 H_{CF}(T)$. **e**, $M(T)$ measured in different applied magnetic fields. When increasing the magnetic field, the ZFC and FC curves start merging at high temperatures.

Figure 4 | Magnetic force microscopy (MFM) images taken at room temperature for the undersurface of the HBD. a, Topography of a 10 μm × 10 μm area of the HBD undersurface, obtained by atomic force microscopy. **b** and **c**, MFM images of the same area, taken at 28 mT and 47 mT, respectively. The frequency shift φ (in degree) represents the strength of the near-surface stray field produced by the HBD.

Figure 5 | Magnetic field- and temperature-induced evolution of the superconducting gap in scanning tunneling microscopy/spectroscopy (STM/S) measurements. a-**c**, Combined topography and zero-bias conductance G_{zb} maps of the HBD undersurface at 0.5 K in different applied magnetic fields. The small patch, remaining blue/green in **c**, is the undoped insulating diamond seed which acted as a

tunneling barrier (see Supplementary Section III) and served as a position marker for our STM/S measurements. **d**, Magnetic field-induced evolution of the characteristic differential conductance spectra taken at location ⊕ in **a**-**c**. The $G_{norm}(V_b)$ curve, measured at B = 0 T, are fitted to the density of states, as obtained from the Maki formalism convoluted with the Fermi distribution function (see Supplementary Section III). **e**, Magnetic field-induced evolution of G_{zb} at different locations. The mean G_{zb} values are calculated by averaging the G_{zb} of 1000 spots around ⊗ and ⊕, respectively. **f**, Temperature-induced evolution of the superconducting gap at locations ⊕ and ⊗. The STM/S data indicate an unusually small surface critical field of ~ 0.3 T in our HBD.

Figure 6 | The correlation between $\rho_{xx}(T)$ and $M(T)$ and the intervention of spin fluctuations in the HBD. a, The $\rho_{xx}(T)$ and $M(T)$ curves are roughly divided into three regions (shadowed in red, green and blue, respectively) with respect to the temperature coefficient of ρ_{xx} and M. The corresponding spin configurations are schematically illustrated in **b**-**d**. **b,** In the temperature window of 100 K < T < $T_{Curie,}$ the overall ferromagnetism of the system results from the ferromagnetic arrangement of the domains (domain walls represented by the black lines). **c**, When T_c < T < 100 K, spin fluctuations intervene in the system via antiferromagnetic arrangement of the domains. **d**, When T < T_c, carriers with antiparallel-aligned spins can be an additional source for Cooper pairing (opposite arrows bound by blue ∞) at the domain walls, in addition to the boron-doping-induced superconductivity in the HBD.

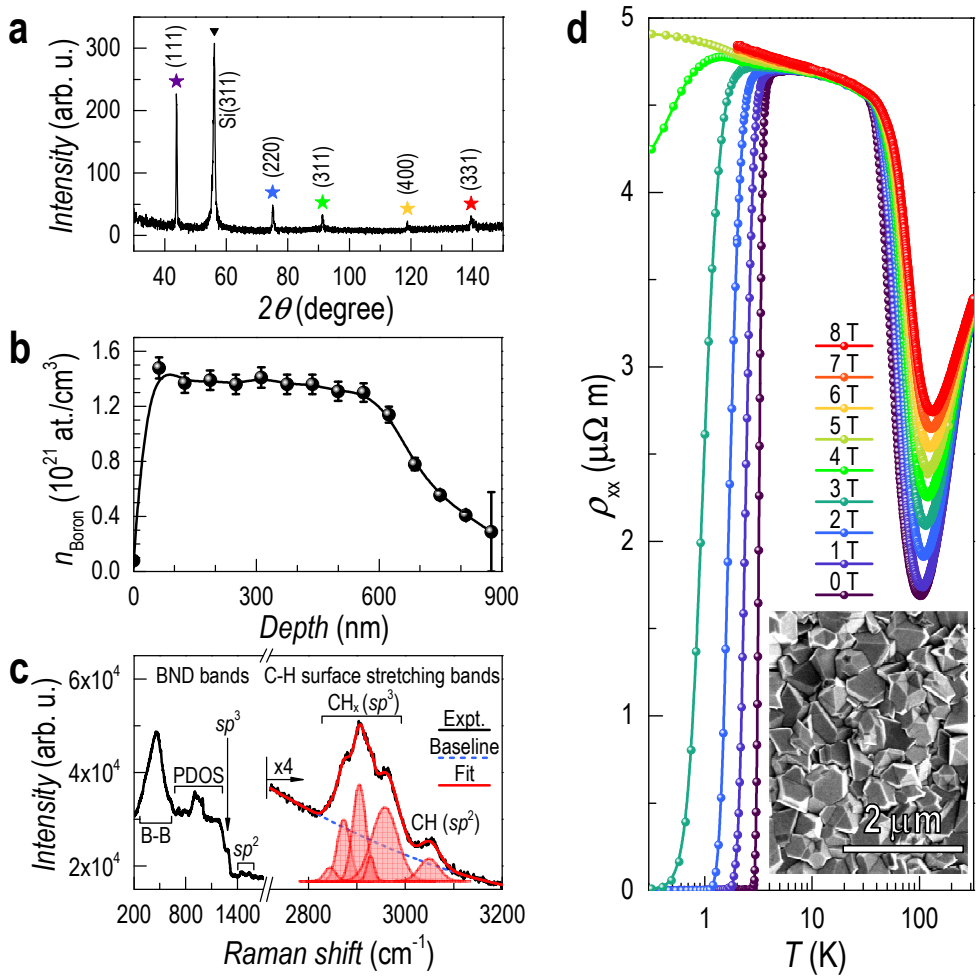
a
Intensity (arb. u.)
(111)
Si(311)
(220)
(311)
(400)
(331)
2θ (degree)
b
n_{Boron} (10^{21} at./cm^3)
Depth (nm)
c
Intensity (arb. u.)
BND bands
C-H surface stretching bands
sp^3
PDOS
B-B
sp^2
CH_x (sp^3)
x4
CH (sp^2)
Expt.
Baseline
Fit
Raman shift (cm^{-1})
d
ρ_{xx} (μΩ m)
8 T
7 T
6 T
5 T
4 T
3 T
2 T
1 T
0 T
2 μm
T (K)

Figure 1

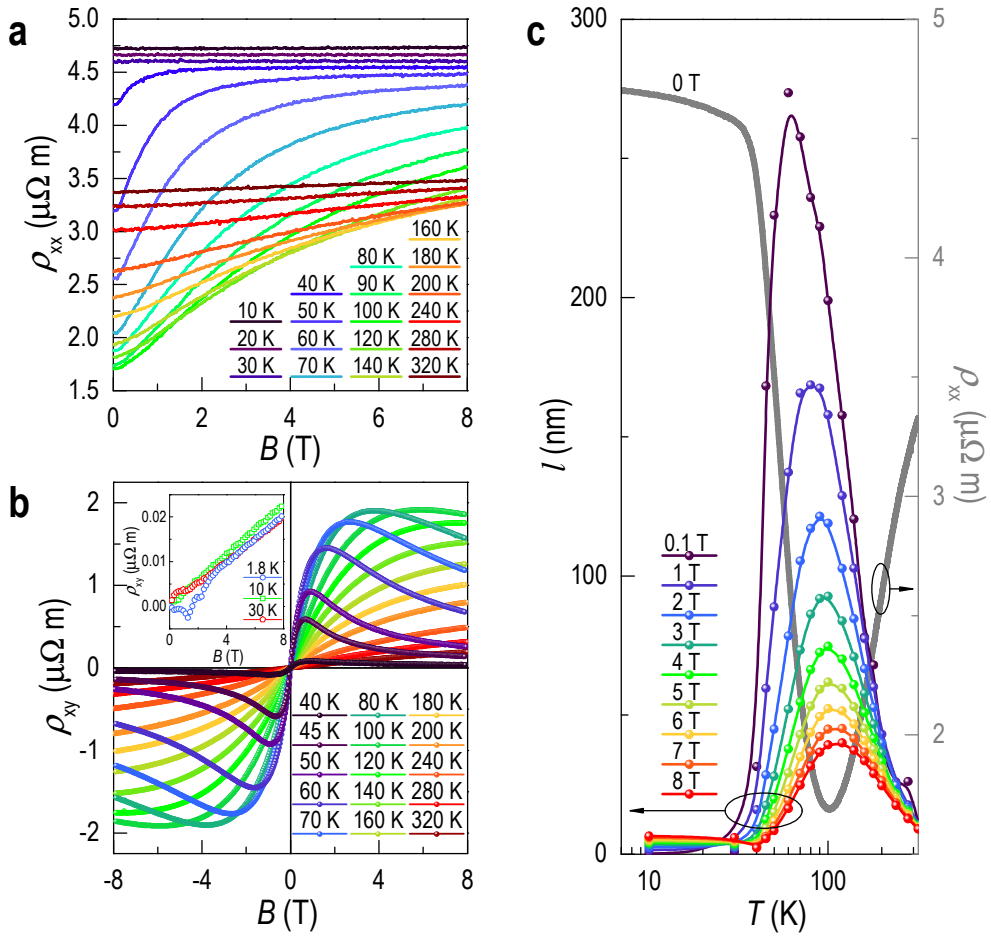
a
b
c
ρ_{xx} (μΩ m)
ρ_{xy} (μΩ m)
B (T)
160 K
80 K
180 K
40 K
90 K
200 K
10 K
50 K
100 K
240 K
20 K
60 K
120 K
280 K
30 K
70 K
140 K
320 K
1.8 K
10 K
30 K
40 K
80 K
180 K
45 K
100 K
200 K
50 K
120 K
240 K
60 K
140 K
280 K
70 K
160 K
320 K
0 T
0.1 T
1 T
2 T
3 T
4 T
5 T
6 T
7 T
8 T
l (nm)
T (K)
ρ_{xx} (μΩ m)

Figure 2

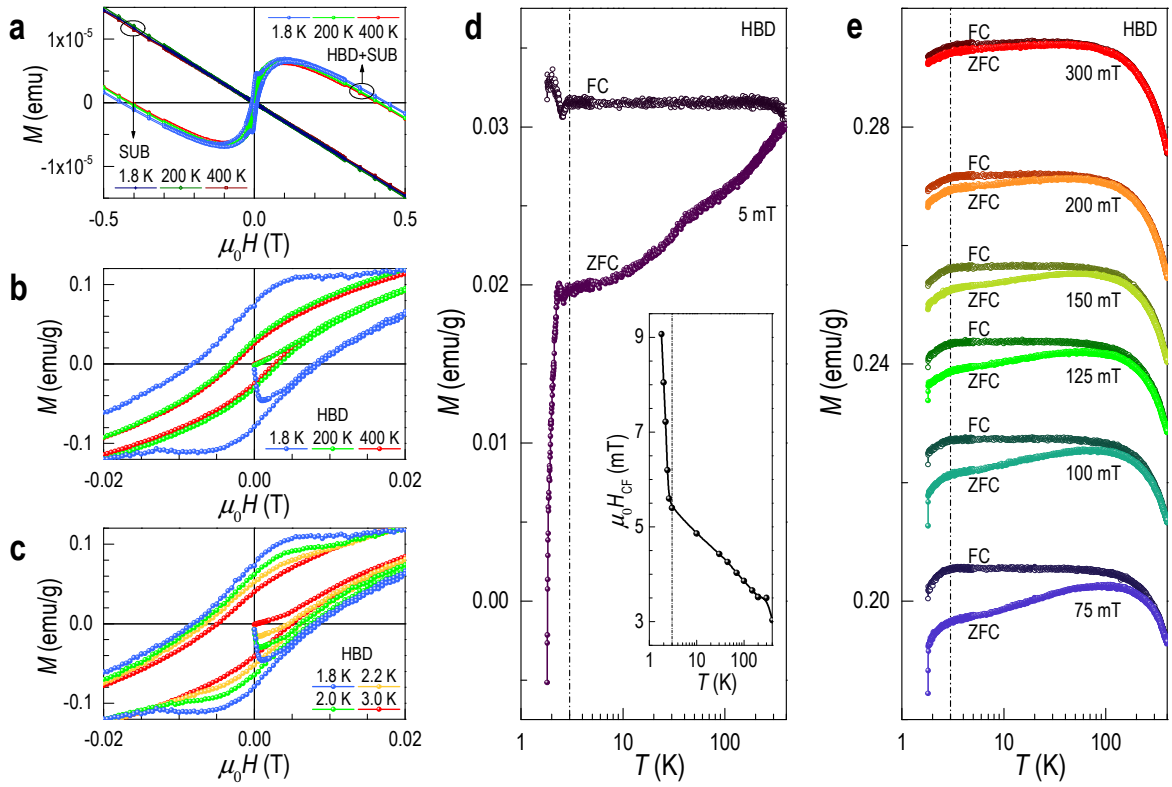
a
1x10-5
0
-1x10-5
M (emu)
1.8 K 200 K 400 K
HBD+SUB
SUB
1.8 K 200 K 400 K
-0.5
0.0
0.5
μ0H (T)
b
0.1
0.0
-0.1
M (emu/g)
HBD
1.8 K 200 K 400 K
-0.02
0.00
0.02
μ0H (T)
c
0.1
0.0
-0.1
M (emu/g)
HBD
1.8 K 2.2 K
2.0 K 3.0 K
-0.02
0.00
0.02
μ0H (T)
d
HBD
FC
ZFC
5 mT
0.03
0.02
0.01
0.00
M (emu/g)
9
7
5
3
μ0HCF (mT)
1
10
100
T (K)
1
10
100
T (K)
e
HBD
FC
ZFC
300 mT
FC
ZFC
200 mT
FC
ZFC
150 mT
FC
ZFC
125 mT
FC
ZFC
100 mT
FC
ZFC
75 mT
0.28
0.24
0.20
M (emu/g)
1
10
100
T (K)

Figure 3

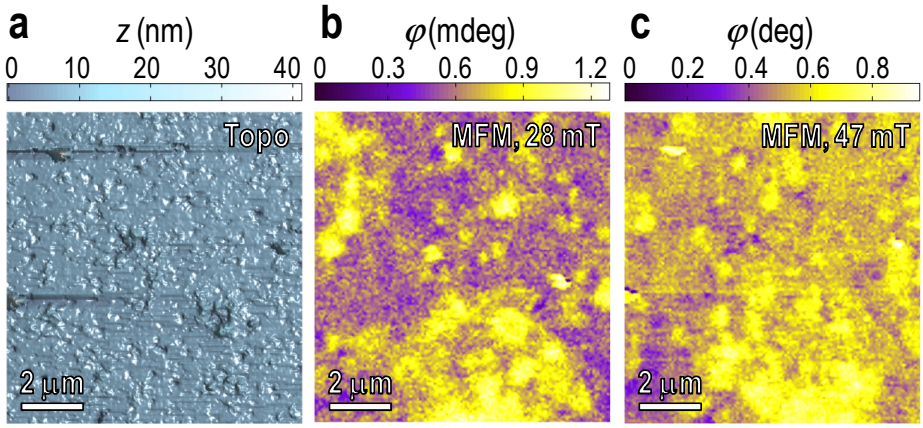
a
z (nm)
0 10 20 30 40
b
φ(mdeg)
0 0.3 0.6 0.9 1.2
c
φ(deg)
0 0.2 0.4 0.6 0.8
Topo
MFM, 28 mT
MFM, 47 mT
2 μm
2 μm
2 μm

Figure 4

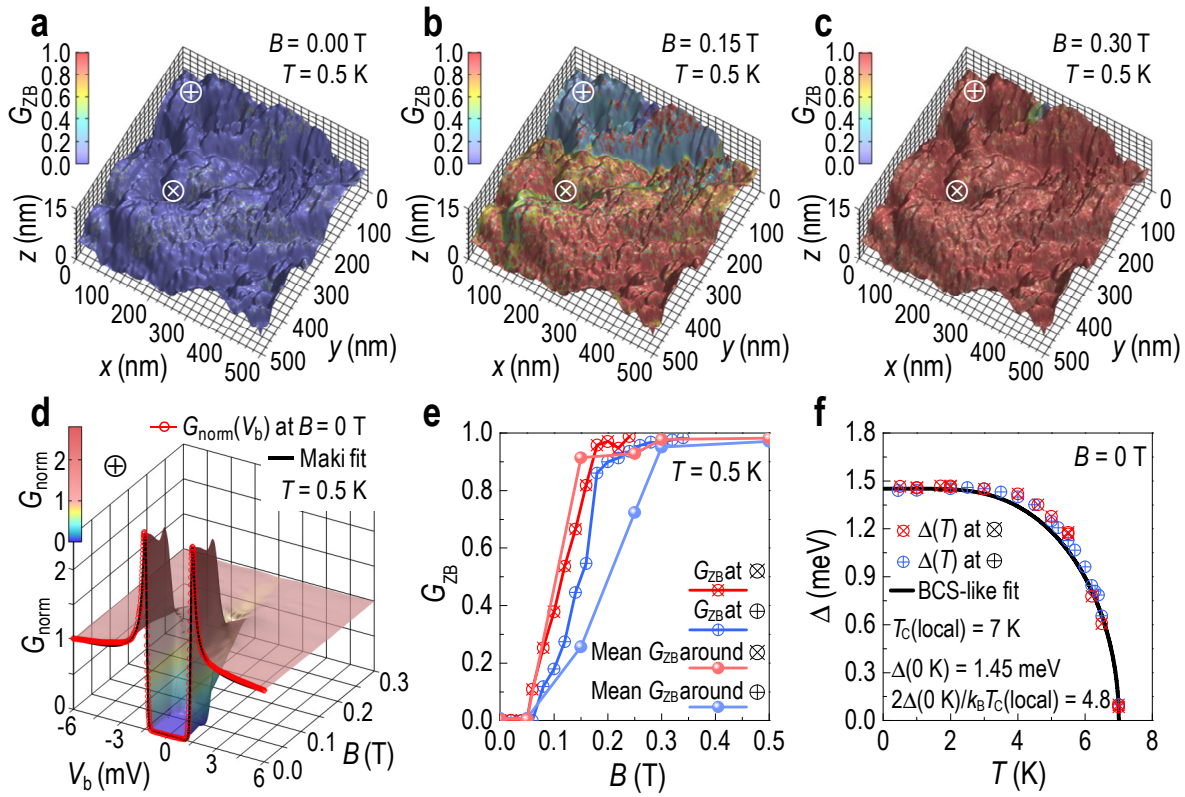
a
b
c
B = 0.00 T
T = 0.5 K
B = 0.15 T
T = 0.5 K
B = 0.30 T
T = 0.5 K
G_ZB
z (nm)
x (nm)
y (nm)
d
e
f
G_norm(V_b) at B = 0 T
Maki fit
T = 0.5 K
G_norm
V_b (mV)
B (T)
G_ZB at ⊠
G_ZB at ⊕
Mean G_ZB around ⊠
Mean G_ZB around ⊕
Δ (meV)
T (K)
Δ(T) at ⊠
Δ(T) at ⊕
BCS-like fit
T_C(local) = 7 K
Δ(0 K) = 1.45 meV
2Δ(0 K)/k_B T_C(local) = 4.8

Figure 5

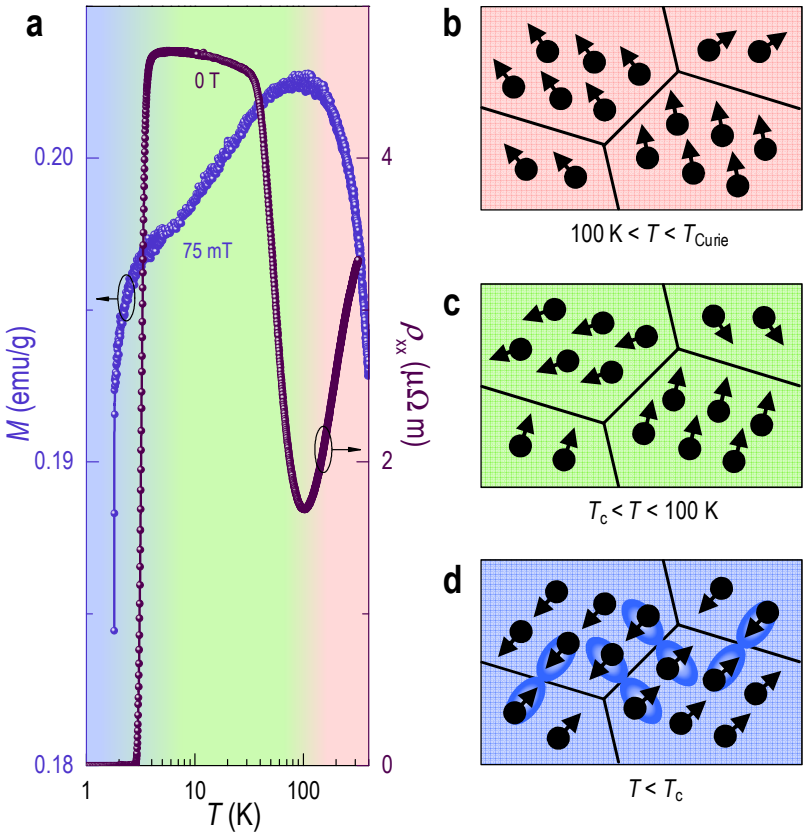
a
0 T
75 mT
0.20
0.19
0.18
M (emu/g)
4
2
0
ρxx (μΩ m)
1
10
100
T (K)
b
100 K < T < TCurie
c
Tc < T < 100 K
d
T < Tc

Figure 6